Available online at www.eccomasproceedia.org
Eccomas Proceedia COMPDYN (2025) 4898-4912

ECCOMAS
Proceedia

COMPDYN 2025
10th ECCOMAS Thematic Conference on
Computational Methods in Structural Dynamics and Earthquake Engineering
M. Papadrakakis, M. Fragiadakis (eds.)
Rhodes Island, Greece, 15-18 June 2025

AI-DRIVEN CRACK ANALYSIS FOR STRUCTURAL HEALTH MONITORING OF ENGINEERING CEMENT COMPOSITE: A LABORATORY STUDY

Azadeh Yeganehfallah[1], Carlo Alberto Avizzano[1], Silvia Caprili[2], and Arash Yeganehfallah[3]

[1] Institute of Mechanical Intelligence, Sant'Anna School of Advanced Studies
Pisa, Italy
azadeh.yeganehfallah@santannapisa.it,carloalberto.avizzano@santannapisa.it

[2] Department of Civil and Industrial Engineering, University of Pisa
Pisa, Italy
silvia.caprili@unipi.it

[2] Structural Research Department, Niroo Research Institute
Tehran, Iran
ayeganeh@nri.ac.ir

Abstract

Engineering Cement Composite (ECC) is a type of high-ductility concrete due to the presence of fibers in its composition. The specific mechanical behavior of ECC shows that under tensile loads, multiple thin cracks are present instead of a single wide one. This feature is known as ECC's crack control capability, which limits the crack width and enhances the durability of the concrete. Hence, ECC is particularly suitable for critical infrastructures such as bridges and tunnels, especially in earthquake-prone regions. In this experimental study, we focus on monitoring ECC samples subjected to controlled loads in a laboratory setting to analyze their cracking behavior using artificial intelligence (AI) techniques. For this purpose, we developed a semantic segmentation model using the Unet architecture to identify cracks within photos of the samples and, subsequently, to measure the crack dimensions using computer vision algorithms. In this investigation, we present an AI-based algorithm that measures the crack width at each point and enables the calculation of the applied load based on this identification with a minimum accuracy of 93.7%. Our experiments show that this technique can segment and measure the crack intensity by producing results that align with real quantifications. The proposed approach offers a reliable and cost-effective tool for structural health monitoring (SHM) of ECC structures as an alternative to the traditional monitoring trends. The proposed algorithms can be integrated with automated techniques, such as using drones during the data collection stage.

Keywords: Engineering Cement Composite, Structural Health Monitoring, Crack Semantic Segmentation, Computer Vision.

ISSN:2623-3347 Published by Eccomas Proceedia.
Peer-review under responsibility of the organizing committee of COMPDYN 2025.
doi: 10.7712/120125.12782.25271

1 INTRODUCTION

Cracks are inevitable in concrete infrastructures due to several factors, including loading, temperature variations, creep, and chemical deterioration mechanisms such as alkali-silicate reactions [1]. These cracks negatively impact mechanical properties, pose safety hazards, and allow aggressive agents to penetrate concrete structures, adversely affecting their durability and service life [2].

A fiber-reinforced cementitious material has been specifically designed to control and limit crack widths, thereby significantly enhancing structures' durability and service life [3-5]. Unlike conventional concrete, ECC exhibits unique strain-hardening behavior, which enables it to sustain additional tensile load even after initial cracking. This results in multiple narrow cracks distributed along the material rather than one large, detrimental crack [6]. Including fibers within the ECC matrix controls crack openings, significantly improves energy dissipation, reduces the risk of sudden failure, and increases the seismic performance of structures [7]. Additionally, ECC is considered environmentally beneficial due to its use of a coal combustion byproduct, fly ash, which enhances long-term strength development and contributes positively to the ECC's self-healing capabilities [6]. The distinct cracking behavior in ECC makes crack analysis and monitoring especially important for structural health assessment. Due to the fiber bridging mechanism, ECC typically exhibits crack spacing of 3–6mm and crack widths around 60μm, which limits crack openings and promotes the formation of multiple secondary cracks [5]. Under flexural loads, ECC demonstrates superior ductility and toughness compared to conventional concrete [8]. During the first loading phase, ECC members experience cracks like traditional concrete; however, with increasing loads, primary cracks do not widen extensively due to the fiber bridging action. Instead, while the external load increases, multiple secondary cracks gradually appear near the initial cracks. Eventually, as secondary cracks saturate, debonding occurs between fibers and matrix, causing a more significant opening of the primary crack, leading ultimately to structural failure. Nonetheless, ECC's flexural strength, ductility, and toughness significantly surpass conventional concretes, providing enhanced resistance to structural failure [9]. This mechanism enhances overall durability and energy dissipation, reducing the risk of catastrophic failures under stress. Accurate monitoring and analysis of these cracks are crucial for assessing structural integrity, predicting future performance, and optimizing ECC structures' maintenance and management strategies [7,10].

Crack shaping monitoring in its conventional format often faces significant limitations, such as being time-consuming [11], high cost, and an evaluation that depends on the engineer's level of knowledge [12]. With the evolution of Artificial Intelligence (AI), a new generation of tools for structural health monitoring has appeared. The combination of AI, Machine learning (ML), and Computer Vision (CV) makes it possible to create an automated inspection machine that surpasses all the barriers of conventional monitoring [13].

Using cameras as an inspection eye that captures structural defects and forwards the image to a well-trained deep learning model to detect, classify, and segment the defect creates an efficient autonomous method for the inspection phase of SHM.

In this paper, we performed an experimental study on monitoring the thickness of shaped cracks on flexural loaded ECC samples using AI technology. To this end, we developed a semantic segmentation model combined with a new loss function named Pixel Average Error Distance (PAED) to segment cracks more precisely in both shape and thickness and, afterward, process computer vision techniques to measure length and thickness.

The paper organization is as follows: after the introduction, we show a related work section where we are going to present the relevant experimental works on ECC material and their methods for the crack analysis and measurements; in section three, we introduce our approach

to shaped crack monitoring and analysis; finally, in the experimental results section, we show the outcome of this approach and compare it with the real-world measures of the crack thickness.

2 RELATED WORKS

Numerous experimental and analytical studies have been conducted to explore the unique mechanical behavior of ECC, particularly its strain-hardening capacity and multiple cracking behavior. Li et al. [7] conducted four-point bending tests on concrete, steel-reinforced concrete, and ECC beams, finding that ECC beams displayed superior ductility and deformation performance. Zhang et al. conducted four-point bending tests on three different types of ECC beams and recorded their first cracking strength, flexural strength, and deflection capacities. Moreover, they recorded the cracking behavior of ECC beams, including the crack number and width in the fixed moment section.

In a comprehensive state-of-the-art review, Hu et al. [6] highlighted ECC's effectiveness in structural strengthening, especially in improving ductility, energy dissipation, and crack control. The review summarized various experimental and numerical works across structural elements and emphasized the material's promising bond performance when hybridized with other reinforcements.

More recently, Zhexin Hao et al. [14] focused on the identification, distribution, and orientation of the fibers in ECC. They showed that the distribution directly affects the crack-bridging properties. Moreover, to have a better understanding of fiber orientation, they developed a method that combines pixel shift multiple-shooting techniques from the computer vision field with semantic segmentation models to automatically and accurately detect and analyze fibers in captured images from cross-sections. The results of their survey show that a fiber orientation of 30 degrees has a notable effect on the bridging behavior of the ECC.

For most laboratory-based case studies, crack monitoring and width measurement have traditionally been conducted manually, which is labor-intensive and prone to inaccuracies.

With the evolution of different computer vision techniques, new methods have been applied to measure the number of cracks and their relative widths. Jiajia et Al., in a recent work (2024), present a crack propagation analysis by using the digital image correlation (DIC) technique in a way that they initially covered the beam surface with a densely scattering spot using a spray, mounting a high-resolution camera to capture synchronous images during the loading process. The crack width was defined based on the distance of the two scattered spots on two sides of the shaped crack edges, corresponding to the initial distance of those spots being captured at the beginning [15].

In the same period, Zhexin Hao et al. 2024 [16] conducted a 3D crack analysis study using X-ray microtomography(μCT) and deep learning semantic segmentation method to develop a highly accurate method to detect, segment, and quantify the 3D format of the cracks in the laboratory scale of ECC samples. They scanned the ECC specimens using high-resolution μCT and achieved the volumetric data with a voxel resolution of 5.4μm. Then, by developing a 3D U-Net, they extracted the 3D geometry of the cracks. They declared that most cracks exhibited thickness in the 20–80μm range, with dominant values around 40μm.

Most existing methods to monitor the ECC structural members are restricted to laboratory conditions based on practical aspects. To make it clearer, they often rely on costly equipment such as X-ray devices and require small-scale specimens with controlled geometries, making them unsuitable for real-world applications in structural health monitoring (SHM).

In contrast, we presented our AI-based approach, which offers flexible, applicable, and cost-effective tools for real-world structural health monitoring. It relies only on basic equipment, such as a standard camera, making it fast, simple, and highly adaptable for real-world use.

3 PROPOSED APPROACH

Our study suggests a joined development of a semantic segmentation model with a computer-vision-based pipeline to detect the shaped cracks on our ECC beam specimens, to segment them, and to quantify their relevant features like the widths. The approach consists of five main stages:

(i) laboratory setup and ECC specimen preparation, (ii) training a deep learning segmentation model, (iii) image acquisition, pre-and post-processing for crack width analysis, and (iv) estimating structural response under loads based on crack widths.

3.1 Laboratory setup and test specimens

The mix proportion used for preparing the ECC specimens was based on the M45 mixture design introduced by Li et al. [17], which has been widely adopted in ECC-related studies [6]. In practice, M45 typically refers to the combination shown in Table 1.

Cement	Fly Ash	Sand	Water	Superplasticizer	PVA fibers
1.0	1.2	0.8	0.56	0.012	2% by volume

Table 1: M45 mixture design.

The four-point bending test was performed according to ASTM C1609 [18] on 360 × 76.2 × 25.4mm beam specimens. The test was carried out at a loading rate of 0.3mm/min when the specimen was 28 days old using a 400KN universal testing machine. Figure 1 shows the recorded mid-span deflection using two vertical Linear Variable Differential Transformers (LVDTs) during the loading process.

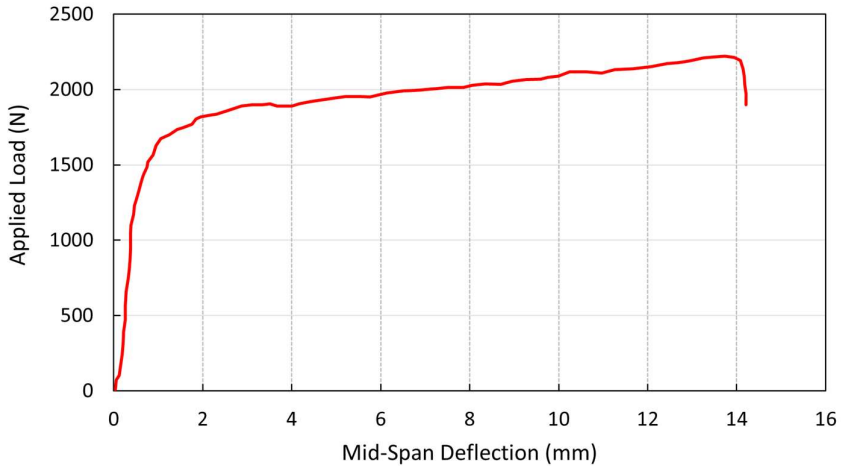

Figure 1: Mid-span stress-strain curve.

3.2 Dataset preparation and deep learning model for semantic segmentation

To measure the crack width, we need to have a clear border of the cracks in the images; in other words, we need a technique that can classify each pixel as crack or non-crack. Semantic segmentation, as a pixel-wise technique, fulfills the desire to create the exact border of the crack. One of the most famous network architectures for semantic segmentation techniques is U-Net. Initially, the architecture was developed for biomedical image semantic segmentation [19].

U-net has two main sides: an encoder part on the left and a decoder side on the right. The encoder is responsible for extracting the multilevel features of the input image; on the other

hand, the decoder generates the prediction mask. The strength point of U-Net is the concatenation process since it preserves spatial information that may be lost during the down-sampling section of the encoding. For the training, we have selected 8594 three-channel images and their corresponding binary mask from CFD [20], CRACK500[21], Cracktree200 [22], Deep Crack [23], Eugen_muller, Forest, GAP, Rissibilder, Sylvie, Volker [24].

We tried to collect different sets of datasets, with different scales of pixel per crack width and various types of textural characteristics to be sure that the model has been generalized in the learning of irregular finest cracks to the wider ones.

We resized (training and validation process) or cropped (test and experimental phase) all the images and their binary masks to the input size of the Unet (128x128 pixels). During the training, we devoted 70 percent of the dataset for the training and 30 percent for the validation part. Elastic deformation as data augmentation is applied to simulate real-world variations and increase model robustness. For this aim, as mentioned in the original U-Net architecture research paper [19], random displacement from a Gaussian distribution with the 10-pixel standard was applied randomly on a grid of 3 by 3. The augmentation was used both for the images and their corresponding mask.

Our training strategy includes initial pre-training of the trained U-Net architecture with the binary cross-entropy loss function (BCE). We have applied the Adam optimizer with a learning rate of 1e-4 and run the training for the 2000 epochs with a batch size of 64.

To fine-tune the model, we have applied our new proposed loss function PAED, inspired by our previously introduced evaluation metric PAED [25]. PAED concentrates on neglecting minor variations in crack locations and preserving the real crack shape. This situation commonly occurs in labeling practice and is penalized heavily with pixel-wise traditional losses [25].

The main structure of the PAED loss function penalizes the distance between the skeletonized predicted mask and the skeletonized ground truth mask. It rewards the predicted pixels that fall inside the original crack region.

For this strategy, we employ the external distance transform of the skeletonized ground truth mask to penalize predictions and the internal distance transform of the original ground truth mask to reward them. In this way, the crack's geometry structure is aligned with its original shape.

The PAED loss function is defined as:

$$PAED = SDF_{GT_{ext}}.\ Skl_{prediction} - \alpha.SDF_{GT_{int}}.Prediction \quad (1)$$

Where:

$SDF_{GT_{ext}} = is\ the\ external\ distance\ map\ of\ the\ skletonized\ ground\ truth\ mask$

$Skl_{prediction} = is\ the\ skletonized\ prediction\ mask$

$SDF_{GT_{int}} = is\ the\ internal\ distance\ map\ of\ the\ fround\ truth\ mask$

$\alpha =$ is a weighting factor (e.g.,10) to emphasize reward for internal matches.

We performed this training experiment using the PyTorch framework (version 2.4.1) with CUDA support on an NVIDIA GeForce RTX 4090 GPU. Table 2 shows the performance metrics of the trained model on the training and validation dataset at epoch 2000.

3.3 Image acquisition, pre-and post-processing, and crack width measurement

To accurately measure the crack's width, we need a tool to convert the pixel scale of the captured image to the real-world scale in millimeters. For this goal, we used an ArUco marker as a defined reference point and placed it adjacent to the ECC specimen so it would be visible

and detected in every frame. ArUco marker playing as a geometric reference, enables calculating the homography matrix(H) to map the frame pixel dimensions to a real-world unit independent of the camera position or the perspective distortion.

Before shooting a frame, we calibrated the Samsung S21 phone camera, using a standard chessboard pattern to correct the lens distortion and improve geometric accuracy. We obtained the camera intrinsic matrix(K) and distortion coefficient (D).

metric	Accuracy	Intersection Over Union (IOU)	PAED Loss
Training set	0.99	0.73	-1650
Validation set	0.982	0.55	-1200

Table 2: Training metrics at epoch 2000.

We captured the frame with a resolution of 2992x2992 under daylight conditions, which is shown in Figure 2. In the first step after capturing the frame, we used these parameters to calculate the homography matrix(H) for image un-distortion and enable the conversion of pixels to real-world measures in mm. We forwarded the image to the trained model to have the segmented cracks in a binary image. Then, the predicted binary masks are undistorted using the H matrix. Binary thresholding is applied to obtain a clear binary vision of the cracks.

Our crack width quantification method is inspired by the correlation-based rotating kernel approach introduced by Jahanshahi et al. [26], which was initially developed for photogrammetry-based structural safety evaluation. In our study, we adapted and modernized this concept using a deep-learning segmentation pipeline and smartphone imaging, making the method significantly more accessible and scalable for laboratory-scale ECC testing scenarios.

To be able to trace all the crack sections and measure their width, we have simulated it as a graph representation. We skeletonized the cracks in their centerline and then converted them to the connected nodes. This conversion allows us to survey all the separate crack branches as a distinct connected component. To accurately measure the local crack width at each skeleton pixel, we systematically rotate a predefined kernel from 0° to 180° and calculate the correlation between the kernel and the predicted mask at each angle. The minimum value indicates the width. In the final step, the pixel level width is converted to real-world scales by applying the H matrix and providing a local crack width measurement. Figure 3 shows the schematic shape of the kernel rotation process on one pixel. The kernel (shown in red) rotates at various angles over the crack mask region (white) to identify the orientation perpendicular to the crack.

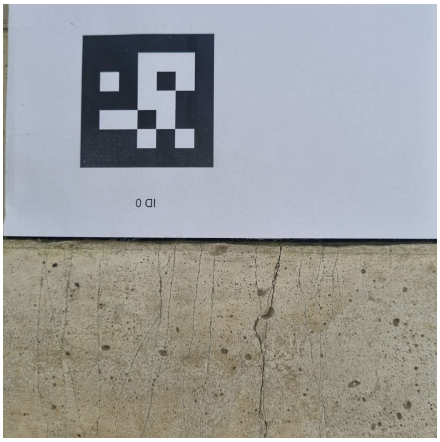

Figure 2: Captured frame of the test specimen.

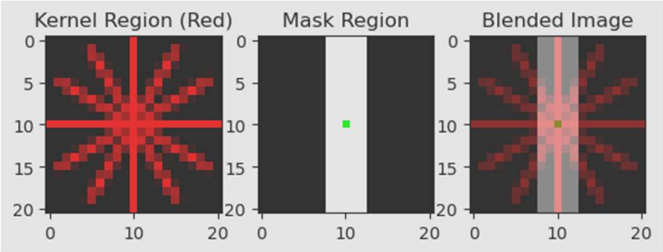

Figure 3: Visualization of the rotating kernel method for crack width measurement.

3.4 Crack width analysis and structural insight

The crack width in ECC beams subjected to flexural loading is considered a key indicator for estimating the tensile strain in the extreme fiber. In a mixture of ECC where PVA fibers are uniformly distributed, when the sample is subjected to four-point bending, the uniform moment conditions between two loading points are happening; it is expected that as the load increases, cracks will develop in a uniformly spaced and uniformly wide manner within this uniform moment region. This occurs due to the crack behavior characteristics of ECC until a crack with the fewest crossing fibers experiences a domino effect that leads to a progressive loss of fiber bridging. Following this failure, the test sample can no longer withstand the load, and the widths of other cracks will reduce due to elastic-plastic behavior.

This behavior is observed in common ECC (specifically M45-ECC) with approximately 2% PVA content. When this amount of fiber is distributed, as mentioned, the spacing of the crack is anticipated to be about 6 to 10 mm. After unloading, the widths of the un-failed cracks return to approximately 0.06 mm. Based on the assumption of linear strain distribution across the section and known stress-strain relationships of ECC in tension and compression [27-30], it is possible to reconstruct stress distribution and calculate the internal moment.

To facilitate theoretical modeling of ECC beams under flexural loading, the following simplifying assumptions are adopted:

1. The tensile behavior of ECC is idealized using a bilinear stress-strain curve, as shown in Figure 4(a).
2. The compressive behavior of ECC is represented by a trilinear stress-strain curve, as shown in Figure 4(b).
3. The plane section remains. The plane assumption is considered valid, meaning that the beam's cross-section remains flat and does not warp under bending, preserving a linear strain distribution.
4. In contrast to conventional concrete, the tensile strength of ECC is taken into account due to its notable strain-hardening and cracking control behavior.

The ECC's tensile stress-strain behavior, illustrated in Figure 4(a), can be described by the following expression, equation 2. Considering the assumptions, this tensile behavior manifests in different strain states, as shown in Figure 5.

$$\sigma_t = \begin{cases} \dfrac{\sigma_{tc}}{\varepsilon_{tc}}\varepsilon & 0 \le \varepsilon < \varepsilon_{tc} \\ \sigma_{tc} + (\sigma_{tu} - \sigma_{tc})\left(\dfrac{\varepsilon - \varepsilon_{tc}}{\varepsilon_{tu} - \varepsilon_{tc}}\right) & \varepsilon_{tc} \le \varepsilon < \varepsilon_{tu} \end{cases} \quad (2)$$

Where:

σ_{tc} = tensile stress at the first crack
ε_{tc} = the strain at the first crack
σ_{tu} = the ultimate tensile stress

ε_{tu} = the tensile strain corresponding to σ_{tu}

The compressive stress-strain relationship of ECC, as illustrated in Figure 4(b), can be expressed as follows:

$$\sigma_t = \begin{cases} 2\dfrac{\sigma_{c0}}{\varepsilon_{c0}}\varepsilon & 0 \le \varepsilon < \dfrac{1}{3}\varepsilon_{c0} \\ \dfrac{2}{3}\sigma_{c0} + \dfrac{\sigma_{c0}}{2\varepsilon_{c0}}\left(\varepsilon - \dfrac{\varepsilon_{c0}}{3}\right) & \dfrac{1}{3}\varepsilon_{c0} \le \varepsilon < \varepsilon_{c0} \\ \sigma_{c0} + (\sigma_{cu} - \sigma_{c0})\left(\dfrac{\varepsilon - \varepsilon_{c0}}{\varepsilon_{cu} - \varepsilon_{c0}}\right) & \varepsilon_{c0} \le \varepsilon < \varepsilon_{cu} \end{cases} \quad (3)$$

Where:

σ_{c0} = the compressive strength

ε_{c0} = the strain at peak stress

σ_{cu} = the ultimate compressive stress (in the post peak branch)

ε_{cu} = the ultimate compressive strain

In this work, we assume $\sigma_{cu} = 0.5\sigma_{c0}$ and $\varepsilon_{cu} = 1.5\varepsilon_{c0}$. To simplify the post-peak compressive response of ECC for analytical modeling. Based on the stress-strain expressions defined in equations (2) and (3), the measured crack widths at the extreme tension fiber can be converted to equivalent tensile strain at each section. Assuming the plane section remains plain under bending, a linear strain distribution across the beam depth can be established. By knowing the vertical crack location, the full strain profile over the cross-section can be inferred through proportional scaling.

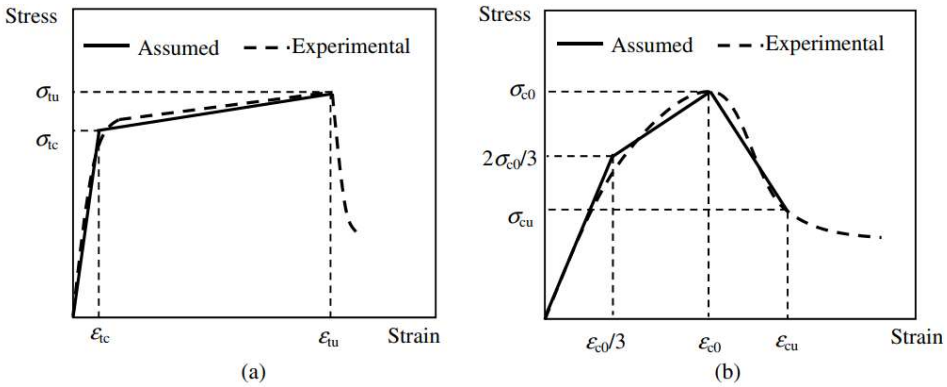

Figure 4: Stress-strain relationship of ECC: (a) under uniaxial tension; (b) under uniaxial compression, [27].

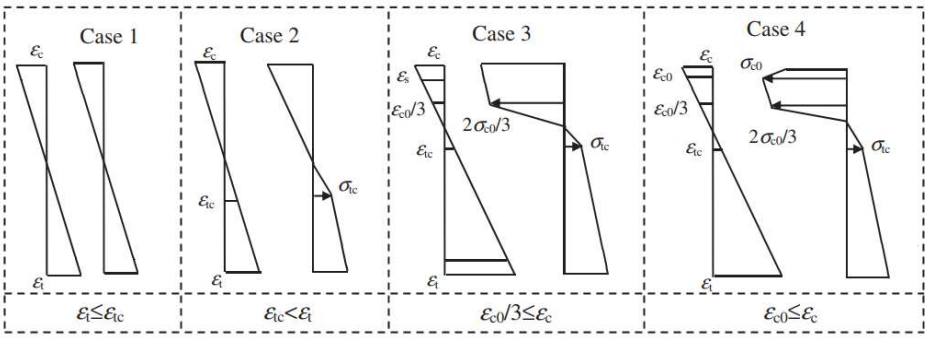

Figure 5: Stress and strain distributions for four distinct stages [27].

Once the strain distribution is determined, the corresponding stress distribution can be calculated using the bilinear and trilinear constitutive laws. This enables the estimation of internal bending moments at different sections along the beam.

For the specific case of our ECC beam subjected to four-point bending, the constant moment region between the loading points allows a straightforward calculation of the applied load from the measured moment.

To approximate the local tensile strain at each crack position, the crack width is divided by the average spacing between adjacent cracks, providing an estimate of the concrete strain at each crack.

The mechanical properties of ECC-M45 used in this study are derived from previous experimental investigations by Li [30]. According to the stress-strain diagram shown in Figure 6, the tensile properties are: $\sigma_{tc} = 4.2\ MPa$, $\varepsilon_{tc} = 0.0015$, $\sigma_{tu} = 4.8MPa$, $\varepsilon_{tu} = 0.038$.

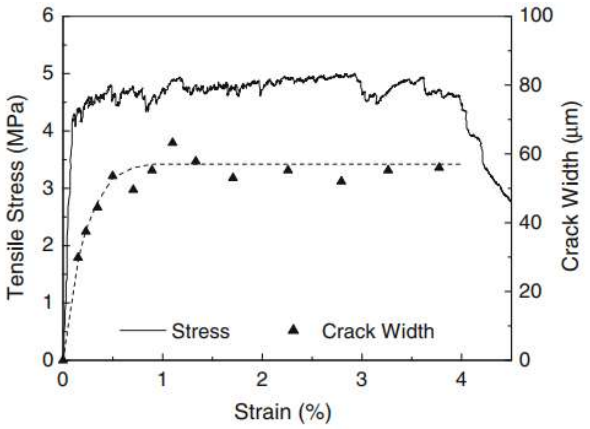

Figure 6: Stress-strain curve and average crack width development of ECC M45 [29].

Additionally, Wang and Li [30] experimentally investigated the compressive behavior of ECC-M45 and reported values of $\varepsilon_{cu} = 0.0043$ and $\sigma_{cu} = 68MPa$, for 28-day-old specimens.

4 EXPERIMENTAL RESULTS

We conducted the experiment on a single ECC specimen, as it sufficiently provided a rich dataset for our comparison of the AI-based crack width measurement approach because of shaping multiple cracks with distinct geometrical characterization.

4.1 Segmentation results and crack width measurement

After the image acquisition and preprocessing, we passed the frame through the trained model and obtained the segmented crack map. The result of applying the post-processing and crack width measurement development is shown in Figure 7, where white lines illustrate the segmented cracks.

To validate the performance of our proposed approach, we manually selected ten points at the same vertical level on the specimen surface on the output screen of the width measurement. The local crack width at each point was computed automatically and displayed in millimeters on the right side of the window. Each value corresponds to the same point color on the sample, presenting a more precise visual mapping between the measurements and the location. To better understand our model performance, we plotted the crack width measures for the ten points with our model output and the manual method in a scatter plot in Figure 8.

According to the selected ten points, we manually measured the width on the same spot on the original specimen surface using a physical crack width ruler and capturing a close-up image for each point. Figure 9

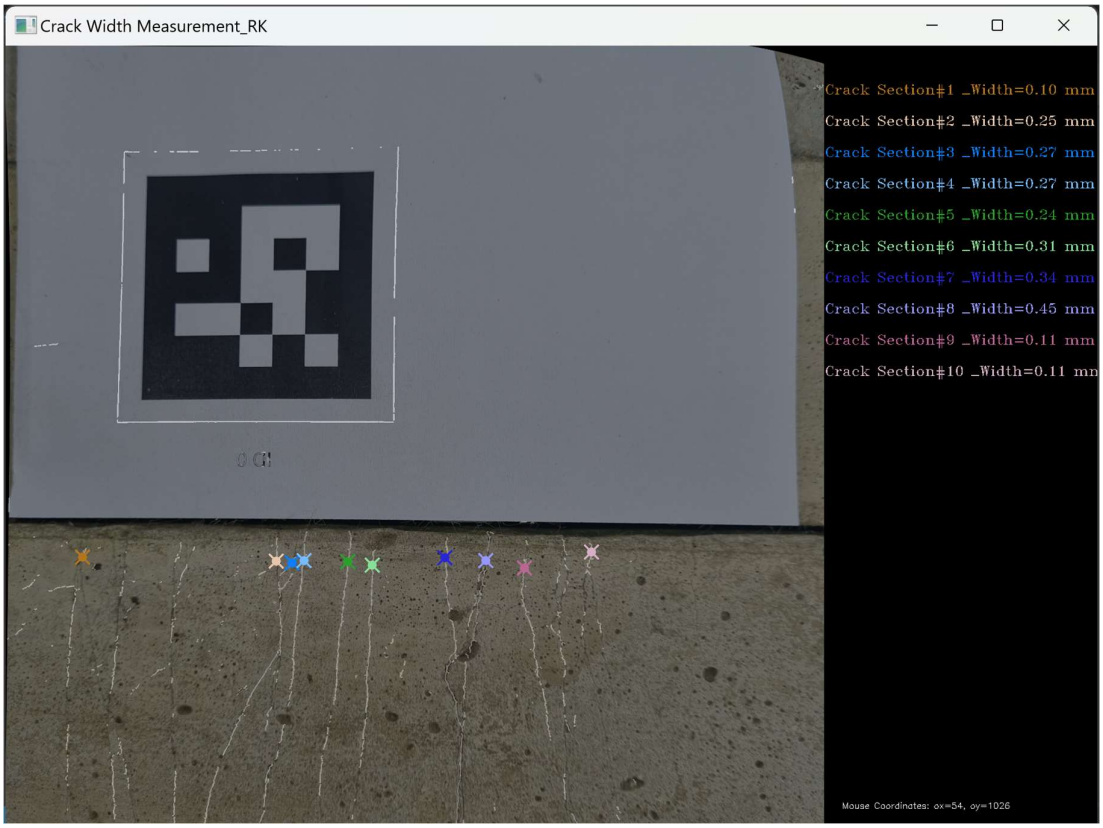

Figure 7: Segmented crack display with 10 annotated points and their corresponding AI-based width measurement.

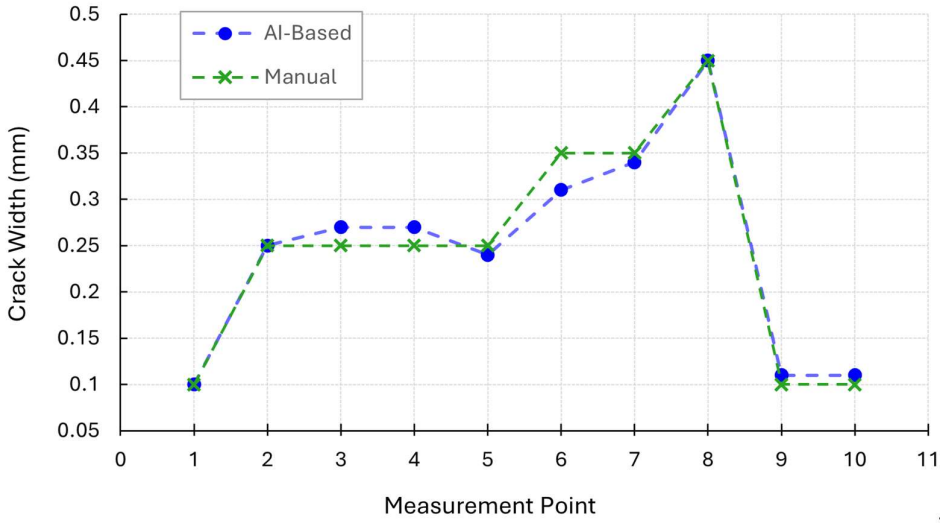

Figure 8: Scatter plot comparison of AI-based method and manual measurement in 10 selected points.

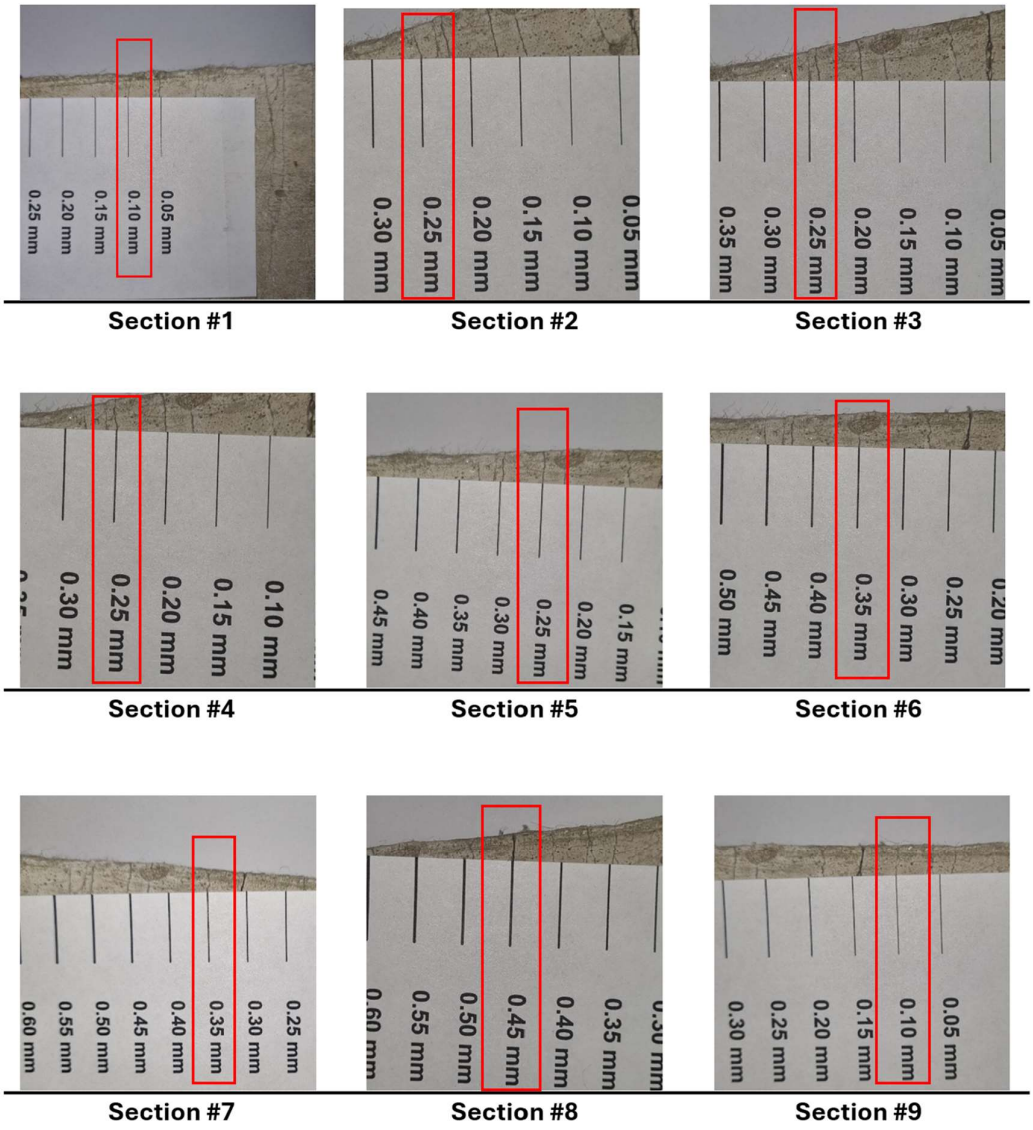

Figure 9: Close-up images of manual crack width measurements.

By inspecting the comparison plot, we found a close correlation between the manual measurements and the AI-based ones. To evaluate the width measurement reliability for estimating applied load, we conducted a worst-case analysis. For this reason, we choose the crack point number six, the one which has the largest error with a real value of 0.04mm. The crack width measured with our AI-based tool is 0.31 mm. To compute the applied load, it is sufficient to reconstruct the strain distribution at the crack location. For achieving the strain distribution, it is necessary to estimate the tensile strain in the extreme tension fiber and measure the vertical extent (height) of the crack across the section.

As described in section 3.4, the strain can be computed, equation (4), by dividing the measured crack width by the average spacing between adjacent cracks, which is 25 mm.

$$\varepsilon_t = \frac{0.31mm}{(25\ mm)/2} = 0.0248 \tag{4}$$

In Figure 10, we illustrate the vertical extent of the crack within the cross-section, the point where the crack vanished. This vanishing point is the actual location of the zero-strain point in the section. Assuming the plane section remains plane after the deformation, the strain distribution can be easily constructed.

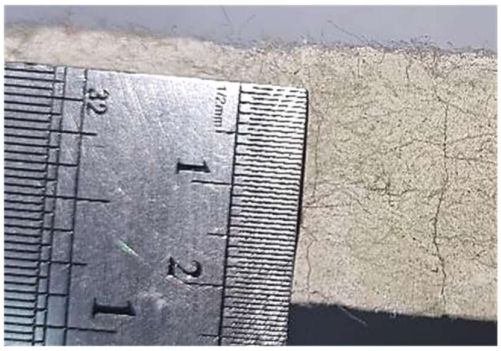

Figure 10. Measuring crack vertical extent in the cross-section.

Figure 11(a) shows the constructed strain distribution across the beam section; utilizing the equation (2) and (3), we can calculate the stress distribution as well. Figure 11(b)
As is evident in Figure 11(b), the stress distributions correspond to case 4 of Figure 5.

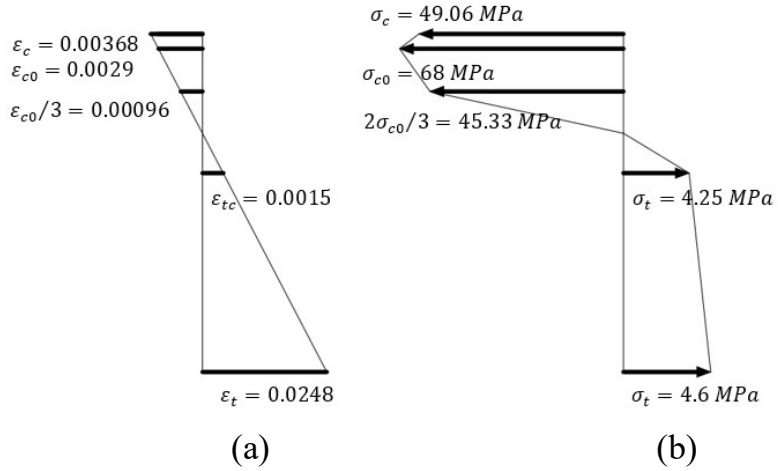

Figure 11. Strain and stress distribution in beam cross-section.

Given that the bending test span configuration was 101.6 mm – 76.2 mm – 101.6mm, the applied load can be calculated from the internal bending moment. In the examined section, based on the obtained stress distribution, the calculated bending moment was 105620.31N-mm, resulting in a corresponding applied load of 2079.13N. Comparing this with the maximum load obtained from the experimental load-displacement curve equal to 2220.532N presented in Figure 1, concludes that the proposed calculation yields a relative maximum error of 6.3%, in a set of ten different samples.

From a structural engineering perspective, the ability to detect and measure such fine cracks using only a camera -with such a low margin of error- denotes this method as strongly promising to overcome the common practices. Achieving around 93–94% accuracy in crack detection shows that the model performs with a very small error, which is noteworthy considering that even in structural design practices, an error margin of 5% is typically acceptable. However, in

the case of existing structures, where we aim to monitor rather than design, achieving such high accuracy is even more significant. In structural health monitoring (SHM), we rarely reach 100% precision due to the limited available information about the object. Therefore, a minimum 93% accuracy rate in crack detection highlights the reliability of the method and shows that it can be used to assess many other structural parameters, such as concrete durability or residual load-bearing capacity of the member. Considering the repeatability property of the technique, it is possible to redo and investigate the required information as many times as needed without further cost, and without intervening the human error. Nevertheless, we highlight that this level of accuracy has been achieved using a basic network architecture and an accessible smartphone camera, indicating that the proposed AI-assisted tool is reliable, executable in real-world SHM processes, and prompt further improvements.

CONCLUSION

In this paper, we did an experimental investigation into automated shaped crack width measurements on an ECC beam specimen, making it possible to estimate the applied load on the ECC structures without traditional manual measurement methods. In ECC members, the crack width, along with crack spacing, provides a practical approximation of localized strain, enabling the estimation of flexural response and, consequently, the applied load.

In our experiment, the ECC specimen was subjected to a four-point bending test, during which multiple cracks were shaped during the test. Our proposed AI-based approach consists of a trained semantic segmentation deep learning model based on U-Net architecture tuned with our novel loss function, PAED, for segmenting the shaped crack and post-processing computer vision pipeline to crack width quantification. Regarding the comparison between the manual measurements at multiple points on the specimen surface and our developed method output for the corresponding points, the proposed method has a very close computation to the real measurements with a worst-case minimum accuracy of 93.7% in applied load computing. This high level of accuracy in SHM applications utilizing one of the most basic deep learning architectures and using a simple phone camera as an eye to capture the situation is particularly noteworthy.

The model could be a foundation for reconstructing structural loading in ECC members as a prediction for long-term structural performance, which establishes a direct link between visual observations and structural mechanics.

REFERENCES

[1] N. Trussell, P. Øystein Nordtug, I. Asadi, M. Kristoffersen, and S. Jacobsen, Water transport in cracks controlled by digital image correlation in wet sprayed concrete with and without an EVA based co-polymer admixture, *Construction and Building Materials*, vol. 400, p. 132423, Oct. 2023

[2] H. C. Ozyildirim, H. Nair, and M. Sharifi, Practical Approaches to Long-Lasting Bridge Decks, Transportation Research Record: *Journal of the Transportation Research Board*, vol. 2678, no. 11, pp. 791–797, May 2024

[3] 5K. R. Lauer and F. O. Slate, Autogenous healing of cement paste, *Materiales de Construcción*, vol. 7, no. 080, pp. 51–51, Apr. 2017

[4] 6 C. Edvardsen, Water permeability and autogenous healing of cracks in concrete, *ACI Materials Journal*, 96(6), 448–455, 1999.

[5] 9J. Zhang, C. K. Y. Leung, and Y. Gao, Simulation of crack propagation of fiber reinforced cementitious composite under direct tension, *Engineering Fracture Mechanics*, vol. 78, no. 12, pp. 2439–2454, Aug. 2011.

[6] 19Z. Hu, M. Elchalakani, S. Yehia, H. Ran, Mohamed Ali Sadakkathulla, and X. Guo, Engineered cementitious composite (ECC) strengthening of reinforced concrete structures: A state-of-the-art review, *Journal of building engineering*, vol. 86, pp. 108941–108941, Jun. 2024.

[7] 10V. C. Li, D. K. Mishra, and H.-C. Wu, Matrix design for pseudo-strain-hardening fiber reinforced cementitious composites*, Materials and Structures*, vol. 28, no. 10, pp. 586–595, Dec. 1995.

[8] Flexural strengthening of reinforced concrete beams using hybrid fibre reinforced engineered cementitious composite, *Engineering Structures*, vol. 284, p. 115992, Jun. 2023.

[9] 13M. Maalej and V. C. Li, Flexural/Tensile‐Strength Ratio in Engineered Cementitious Composites, *Journal of Materials in Civil Engineering*, vol. 6, no. 4, pp. 513‐528, Nov. 1994.

[10] 20X. Shang, J. Yu, L. Li, and Z. Lu, Strengthening of RC Structures by Using Engineered Cementitious Composites: A Review, *Sustainability,* vol. 11, no. 12, p. 3384, Jun. 2019.

[11] R. Stricker et al., Road Surface Segmentation - Pixel-Perfect Distress and Object Detection for Road Assessment. *IEEE 17th International Conference on Automation Science and Engineering (CASE)*, Lyon, France, Aug. 2021.

[12] M. Żarski, B. Wójcik, and J. A. Miszczak, KrakN: Transfer Learning framework and dataset for infrastructure thin crack detection, *SoftwareX,* vol. 16, p. 100893, Dec. 2021.

[13] Sattar Dorafshan, M. Maguire, N. V. Hoffer, and C. Coopmans, Challenges in bridge inspection using small unmanned aerial systems: Results and lessons learned, *International Conference on Unmanned Aircraft Systems*, Miami Marriott Biscayne Bay, Miami, FL, Jun. 2017.

[14] Z. Hao, Z. Li, J. Wang, C. Lu, and B. Dong, High-precision full-field fiber identification and distribution analysis in engineered cementitious composite (ECC) through computervision, *Construction and Building Materials*, vol. 462, p. 139974, Feb. 2025.

[15] J. Zhou, G. Xia, P. Wang, J. Zhao, L. Xu, and J. Pan, Investigation of flexural cracks in engineered cementitious composites beams reinforced with CFRP bars*, Construction and Building Materials*, vol. 438, pp. 136900–136900, Jun. 2024.

[16] Z. Hao, Z. Li, J. Wang, C. Lu, and B. Dong, High-precision full-field fiber identification and distribution analysis in engineered cementitious composite (ECC) through computervision, *Construction and Building Materials*, vol. 462, p. 139974, Feb. 2025.

[17] V. Li, Engineered cementitious composites (ECC): bendable concrete for sustainable and resilient infrastructure. Berlin, Germany: Springer, 2019.

[18] ASTMC1609, Standard Test Method for Flexural Performance of Fiber-Reinforced Concrete; *ASTM International: West Conshohocken*, PA, USA, 2011.

[19] O. Ronneberger, P. Fischer, and T. Brox, U-Net: Convolutional networks for biomedical image segmentation, *arXiv (Cornell University)*, May 2015.

[20] Y. Shi, L. Cui, Z. Qi, F. Meng, and Z. Chen, Automatic Road Crack Detection Using Random Structured Forests, *IEEE Transactions on Intelligent Transportation Systems*, vol. 17, no. 12, pp. 3434–3445, Dec. 2016.

[21] L. Jiang, Y. Xie, and T. Ren, "A Deep Neural Networks Approach for Pixel-Level Runway Pavement Crack Segmentation Using Drone-Captured Images," Jan. 09, 2020.

[22] Q. Zou, Y. Cao, Q. Li, Q. Mao, and S. Wang, CrackTree: Automatic crack detection from pavement images, *Pattern Recognition Letters*, vol. 33, no. 3, pp. 227–238, Feb. 2012.

[23] Y. Liu, J. Yao, X. Lu, R. Xie, and L. Li, DeepCrack: A deep hierarchical feature learning architecture for crack segmentation, *Neurocomputing*, vol. 338, pp. 139–153, Apr. 2019.

[24] K. Ha, "khanhha/crack_segmentation," GitHub, Feb. 21, 2024.

[25] A. Yeganehfallah, C. A. Avizzano, and S. Caprili, Automated Crack Identification, to Ease Maintenance of Reinforced Concrete Bridges, *Procedia Structural Integrity*, vol. 62, pp. 201–208, 2024.

[26] M. R. Jahanshahi and S. F. Masri, "A new methodology for non-contact accurate crack width measurement through photogrammetry for automated structural safety evaluation," *Smart Materials and Structures*, vol. 22, no. 3, p. 035019, Feb. 2013.

[27]]. F. Yuan, J. Pan, and C. K. Y. Leung, "Flexural Behaviors of ECC and Concrete/ECC Composite Beams Reinforced with Basalt Fiber-Reinforced Polymer," *Journal of Composites for Construction*, vol. 17, no. 5, pp. 591–602, Oct. 2013.

[28] M. Kh, M. Özakça, and T. Ekmekyapar, "Akademia Baru Numerical and Parametric Studies on Flexural Behaviour of ECC Beams by Considering the Effect of Slag and Micro-PVA Fibre," *Journal of Advanced Research in Applied Mechanics* ISSN, vol. 21, no. 1, pp. 2289–7895, 2016, Accessed: Apr. 09, 2025.

[29] V. C. Li, "Tailoring ECC for Special Attributes: A Review," *International Journal of Concrete Structures and Materials*, vol. 6, no. 3, pp. 135–144, Sep. 2012.

[30] Wang, Shuxin, and Victor C. Li. "Polyvinyl alcohol fiber reinforced engineered cementitious composites: material design and performances." Proc., *Int'l Workshop on HPFRCC Structural Applications*, Hawaii. 2005.